Gravitational instability due to the dissolution of carbon dioxide in a Hele-Shaw cell

A. Vreme,[1,3] F. Nadal,[2] B. Pouligny,[1] P. Jeandet,[4] G. Liger-Belair,[3] and P. Meunier[5]
[1]*Centre de Recherche Paul Pascal, UPR CNRS 8641, 33600 Pessac, France*
[2]*Commissariat à l'energie atomique, 33314 Le Barp, France*
[3]*Groupe de Spectroscopie Moléculaire et Atmosphérique, UMR CNRS 7331, Université de Reims Champagne-Ardenne, Post Box 1039, 51687 Reims, France*
[4]*Unité de Recherche sur la Vigne et le Vin de Champagne, EA 4707, Université de Reims Champagne-Ardenne, Post Box 1039, 51687 Reims, France*
[5]*Institut de Recherche sur les Phénomènes Hors Équilibre, UMR CNRS 7342, Aix-Marseille Université, 13013 Marseille, France*
(Received 25 April 2016; published 28 October 2016)

We present an experimental study of the gravitational instability triggered by dissolution of carbon dioxide through a water-gas interface. We restrict the study to vertical parallelepipedic Hele-Shaw geometries, for which the thickness is smaller than the other dimensions. The partial pressure of carbon dioxide is quickly increased, leading to a denser layer of CO_2-enriched water underneath the surface. This initially one-dimensional diffusive layer destabilizes through a convection-diffusion process. The concentration field of carbon dioxide, which is visualized by means of a pH-sensitive dye, shows a fingering pattern whose characteristics (wavelength and amplitude growth rate) are functions of the Rayleigh (Ra) and the Darcy (Da) numbers. At low Rayleigh numbers, the growth rate and the wave numbers are independent of the Rayleigh number and in excellent agreement with the classical results obtained numerically and theoretically in the Darcy regime. However, above a threshold of $\mathrm{Ra}\sqrt{\mathrm{Da}}$ of the order of 10, the growth rate and the wave number strongly decrease due to the Brinkman term associated with the viscous diffusion in the vertical and longitudinal directions. In this Darcy-Brinkman regime, the growth rate and the wave number depend only on the thickness-based Rayleigh number $\mathrm{Ra}\sqrt{\mathrm{Da}}$. The classical Rayleigh-Taylor theory including the Brinkman term has been extended to this diffusive gravitational instability and gives an excellent prediction of the growth rate over four decades of Rayleigh numbers. However, the Brinkman regime seems to be valid only until $\mathrm{Ra}\sqrt{\mathrm{Da}} = 1000$. Above this threshold, the transverse velocity profile is no longer parabolic, which leads to an overestimation of the wave number by the theory.

DOI: 10.1103/PhysRevFluids.1.064301

I. INTRODUCTION

In order to reduce the emission of gases causing greenhouse effects, it has been proposed for a long time to store carbon dioxide (CO_2) in saline aquifers. This solution mainly relies on the process of dissolution of CO_2 in water through a porous medium. Indeed, the molecular diffusion of CO_2 into water is very slow, which strongly limits the maximum injection rates allowed for geoengineers. Fortunately, the injected CO_2 spreads beneath a caprock and is then subject to gravitational (or convective) and fingering instabilities, which highly accelerates the process of dissolution [1]. The viscous fingering instability which occurs in a porous medium (often modeled by a Hele-Shaw cell) due to a viscosity variation has been widely studied experimentally and theoretically [2]. We will focus in this paper on the gravitational instability occurring in saline aquifers. Indeed, the dissolution of CO_2 in the salted water creates a denser layer of CO_2 saturated brine at the top of the pure brine. The destabilization of this layer creates a convective mixing of CO_2 in the nonlinear regime [3], which strongly accelerates the solubility trapping of CO_2.

Various authors addressed the problem of the stability of a diffuse denser layer from both analytical and numerical points of view. Rees *et al.*'s review article [4] gathers the main contributions in two-dimensional porous media. The layer is stable at the beginning of the dissolution process and becomes unstable after a time which has been evaluated numerically [3,5,6] and analytically [7–9]. The large variation of a factor 3 for the reported values of this onset time is mostly due to the fact that the growth rate highly depends on the norm used to measure the amplitude of the perturbation [10]. However, the scalar flux at the free surface remains diffusive in the linear stage of the instability [3]. It is only in the nonlinear regime of the instability that the convective processes enhance the scalar flux, with a very weak difference between the two- and three-dimensional (2D and 3D) simulations [11]. The onset time of the nonlinear regime is thus the most interesting quantity for geophysical applications. This onset time has been measured numerically [3,5,11,12] and highly depends on the amplitude of the perturbation [8] but also on the time at which the perturbation is applied [13].

However, there are very few experimental studies using real CO_2 dissolved in a porous medium. Kneafsey and Pruess [14] presented results at low Rayleigh numbers for CO_2 dissolution in water at 4 MPa in a Hele—Shaw cell. Outeda *et al.* [15] studied the case of larger Rayleigh numbers. However, they mainly focused on the role of the pH-sensitive indicator used to visualize the destabilization pattern and only a fraction of decade in Rayleigh number was explored. Several authors proposed alternative model systems to mimic convection enhanced CO_2 dissolution in porous media (saline aquifers). Backhaus *et al.* [16] proposed a model system composed of water and propylene glycol (the former and the latter replacing the carbon dioxide and the brine, respectively) and Neufeld *et al.* [17] used a mixture of methanol and ethylene glycol to mimic supercritical CO_2, the lower fluid being pure water. Both studies were done at large Rayleigh numbers. Slim *et al.* [18] used $KMnO_4$ particles in contact with water as an analog for carbon dioxide in contact with a brine along a flat interface. They showed that the amplification of the perturbation amplitude was close to the analytical predictions.

However, there is *a priori* no reason to see a good agreement between the numerical simulations and the Hele-Shaw experiments at high Rayleigh numbers. Indeed, the Darcy equations used in the simulations describe the flow of a Hele-Shaw cell at low Rayleigh numbers only. At large Rayleigh numbers, the viscous terms in the horizontal and vertical directions are not negligible [19] and should be added to the Darcy equations. Zeng *et al.* [20] showed that this Brinkman correction [21] comes from nonlocal terms but that it can be reduced to the viscous shear stress of the gap-averaged velocity at long wavelengths. The Darcy-Brinkman model has been used in the case of Rayleigh-Bénard convection [22]. It has also been used in the case of the miscible Rayleigh-Taylor instability [19] and showed a good agreement with experimental results obtained for two semi-infinite miscible fluids [23]. However, three-dimensional (3D) numerical stability results [24] showed that the flow within the Hele-Shaw cell is no longer parabolic for very large Rayleigh numbers, such that the Darcy-Brinkman model is only valid in an intermediate regime. Finally, Martin *et al.* [25] showed that the inertia term may be kept in the Brinkman model by simply averaging the Navier-Stokes equations over the cell width. This 2D Navier-Stokes-Darcy model (NSD) gives a very good prediction of the growth rate when compared to the numerical simulations of the full 3D Navier-Stokes equations at low Schmidt numbers.

The goal of this paper is to determine the range of Rayleigh numbers in which the Darcy model is valid for the gravitational instability of a diffusing layer. This is done using careful comparisons between theory and experiments in the linear regime. Materials and methods are depicted in Sec. II. Experimental results are presented in Sec. III and interpreted in the scope of a simplified theory. Main results are summarized in Sec. IV.

II. MATERIALS AND METHODS

A. Experimental setup

The details of the experimental setup are accessible in Ref. [26] and only the main characteristics are given below. The core of the experimental setup is shown in Fig. 1(a). It mainly consists of

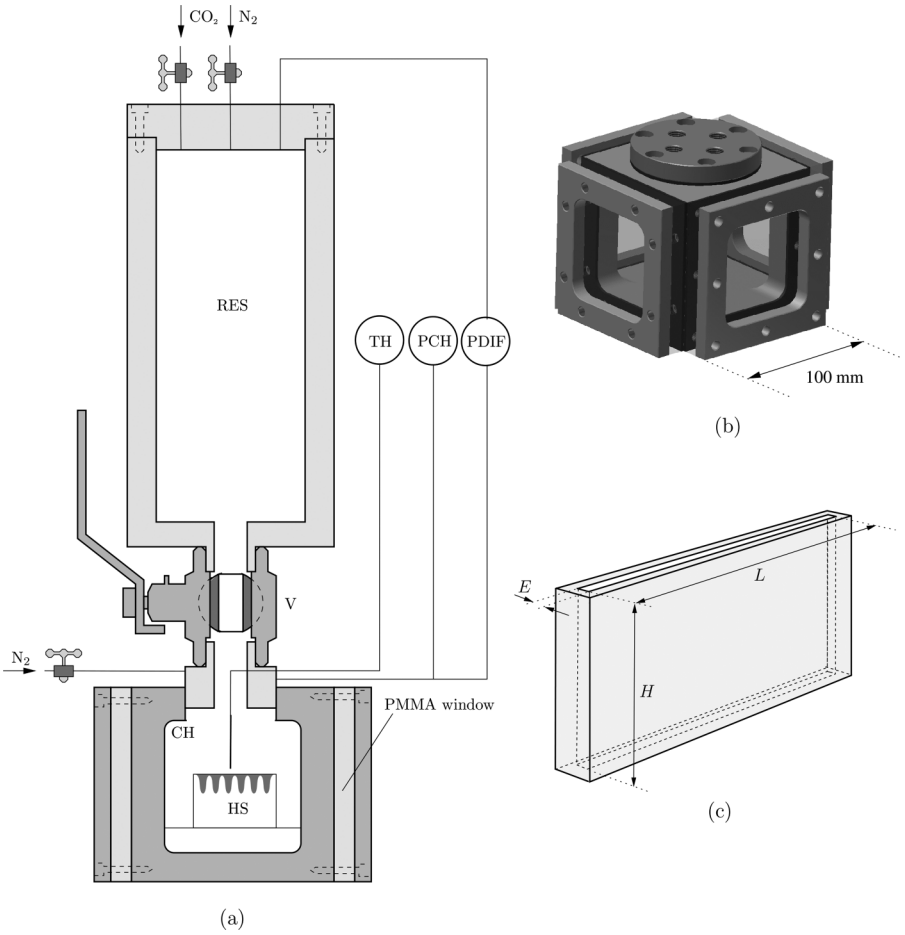

FIG. 1. Geometry of the experimental setup. (a) General view: reservoir, RES; main chamber, CH; ball valve, V; differential pressure sensor, PCH; differential pressure sensor, PDIF; thermocouple, TH; and Hele-Shaw cell, HS. (b) Cubic pressure chamber, CH, housing the Hele-Shaw cell. (c) Hele-Shaw glass cell (dimensions $E \times H \times L$).

a parallelepipedic glass cell (Hele-Shaw cell, HS) filled with water and placed at the center of an aluminium chamber [CH; see Fig. 1(b)]. The contact line is pinned thanks to sharp edges so that in most cases the meniscus can be considered as flat. Dimensions of the cells which we used in our experiments are given in Table I. It should be noted that the height of the Hele-Shaw cell H is relatively small in order to fit within the pressure chamber. Moreover, the thickness E is

TABLE I. Dimensions of parallelepipedic glass cells purchased from Optik-C (France).

Da	Width L (mm)	Thickness E (mm)	Height H (mm)	Pressure P_{CO_2} (bar)
1.33×10^{-6}	70.0	0.2	50.0	3.2; 6.4
8.33×10^{-6}	70.0	0.5	50.0	0.2; 0.4; 0.8; 1.6; 3.2; 6.3
2.70×10^{-5}	70.0	0.9	50.0	0.2; 0.4; 0.8; 1.6; 3.2; 6.3
2.08×10^{-4}	60.0	2.0	40.0	0.05; 0.1; 0.2; 0.4; 0.8; 1.6; 3.2; 6.3
1.30×10^{-3}	60.0	5.0	40.0	0.4; 0.8; 1.6; 3.2; 6.3

relatively large, up to 5 mm, such that the aspect ratio H/E can be as small as 8. This allows us to cover completely the Darcy-Brinkman regime. The temperature in the chamber is assessed using a thermocouple (TH) located close to the free surface of the Hele-Shaw cell.

The present experimental setup is an extension of the one used to study the stationary plume induced at late stages by dissolution of carbon dioxide in a cylinder filled with water [27]. In the present case, we focus on the early stages of the gravitational instability.

A technical difficulty is that direct compression of the gas inside the chamber in general causes a raise in temperature, which in turn causes a purely thermal convection inside the liquid. For instance, whereas the formation of a denser CO_2 charged layer under compression makes the fluid unstable, a local raise in temperature (close to the free surface) could induce a vertical stabilizing temperature gradient. Conversely, horizontal temperature gradients could enhance the destabilization due to dissolution and consequently perturb the effect we wish to characterize, since horizontal thermal gradients are unconditionally unstable [28]. The experimental setup has thus been modified to enable carbon dioxide intake without any pressure change by means of the following operating procedure. The main chamber (of volume $V_C = 743\ \text{cm}^3$) is initially filled with nitrogen at a given total pressure P_T varying from 1 to 14 bars. A large reservoir (of volume $V_R = 1570\ \text{cm}^3$) is filled with carbon dioxide with a total pressure $P_T + \delta P$ slightly greater than P_T (with $\delta P \sim 0.01$ bar $\ll P_T$). This allowed a rapid intake of CO_2 in the chamber when the valve is open with a negligible temperature rise. In our case, the mixing time has been measured (by means of infrared techniques) to be 35 ± 5 s, which is much smaller than the growth time of the gravitational instability. The final partial pressure of CO_2 is given by $P_{CO_2} = (V_C + V_R + V_V)P_T/V_R$, where V_V is the volume of the valve.

B. Measurement techniques

Both experimental techniques detailed below (particle image velocimetry and laser-induced fluorescence) require the use of a laser sheet generated from a classical laser beam (Coherent Genesis, USA) at 514 nm in wavelength (green), through reflection onto a rotating mirror. The rotating mirror is located at the front focal plane of a cylindrical lens. The laser sheet inside the tank is thus made of a horizontal ray rapidly scanned (at 1 kHz) from bottom to top and is almost uniform with a power of about 780 μW cm^{-1}. An optional cylindrical lens, which slightly focuses the laser beam in horizontal planes, reduces the thickness of the laser sheet from 1270 to 164 μm.

As dissolution of CO_2 in water lowers the pH of the solution, the concentration field of dissolved gas can be easily revealed by means of a pH-sensitive dye. For this purpose, we use fluorescein (free acid, Sigma-Aldrich, USA), which is well known as a fluorescent pH probe [29–31]. In all our experiments, the fluorescein concentration is 1.6×10^{-6} M L^{-1}. We only use laser-induced fluorescence (LIF) as a qualitative tool, insofar as we only need to detect the wavy deformation of the diffuse CO_2 layer at the onset of chemoconvection. Note that performing a real quantitative assessment of the isoconcentration curves would be an arduous task (due, among other factors, to the extremely nonlinear response of the fluorescence to a change in carbon dioxide concentration), which lies far beyond our needs.

We perform measurements of the flow fields using particle image velocimetry (PIV). Convection flows are made visible by adding tracer particles in the fluid. For measurements of the tangential components of the velocity (i.e., with the laser sheet parallel to the main walls of the Hele-Shaw cell), we use polystyrene spherical particles (polybead microspheres, Polysciences, Inc, USA), 4.5 μm in diameter, at very low concentration ($\rho_p \sim 18.75 \times 10^{-12}$ g cm^{-3}). For transverse PIV measurements (i.e., with the laser sheet normal to the main walls of the Hele-Shaw cell), the concentration of tracers is five times higher. The settling velocity of the particles, which is of the order of 1.8 μm/s, is negligible compared to the velocity of the fluid during the instability (ranging from 0.1 to 5 mm/s).

We use two video cameras to grab PIV and LIF image sequences. The PIV camera (PixelflyQE, PCO, Germany), which is placed behind a green interference filter, records images with a 1024×1368 resolution with a frame rate of 10 fps in usual conditions. Image sequences of the tracers are

eventually processed using a cross-correlation routine optimized for large velocity gradients [32]. The LIF camera is an analog low-light-level camera (Hamamatsu C5985-10, Japan). The orange light from the fluorescein is reflected onto a dichroic mirror and further filtered through an orange filter. The analog video signal is transformed into digital images (739×575 resolution, 10 bits) by means of a frame grabber (NI PCI 1409, National Instruments, USA) and exploited with a homemade routine. Because the fluorescence is very faint, it is necessary to accumulate photoelectrons to obtain acceptable gray level values. So, in general, the frame rate is only 1 fps.

We carefully checked that there was no noticeable modification of the experimental results due to the presence of fluorescein and tracers by varying the concentration of the fluorescein over three orders of magnitude and by comparing experiments with and without PIV particles and with and without fluorescein.

C. Basic equations and nondimensional parameters

In porous media, the velocity scale $\mathcal{U}$ is given by the equilibrium between the gravity force and the viscous term

$$\mathcal{U} = \frac{K \Delta\rho g}{\mu}. \tag{1}$$

The permeability K is taken equal to $E^2/12$ (note that this is only valid at low Rayleigh numbers in a Hele-Shaw cell). The density difference $\Delta\rho = \alpha k_H P_{CO_2} \rho_0$ is the product of the chemical expansion coefficient of the density $\alpha = (1/\rho_0)(\partial\rho)/(\partial C)$, the Henry's constant k_H of CO_2 in water, and the partial pressure of CO_2. The product αk_H has been measured by Hebach *et al.* [33] but their results are marred by a large uncertainty $\alpha k_H = 0.004 \pm 0.001\,\mathrm{MPa}^{-1}$, which leads to a large uncertainty of the order of 25% on the experimental determination of the Rayleigh number. The permeability K is taken equal to $E^2/12$ since this is obtained for a parabolic flow in a Hele-Shaw cell. g is the acceleration due to gravity and $\mu = \nu\rho_0$ is the dynamic viscosity (with $\nu = 1 \pm 0.02 \times 10^{-6}\,\mathrm{m^2\,s^{-1}}$).

In porous media, there are two possible choices for the length scale of the problem. It first appears natural to take the cell height H. This dimensionalization is useful at late times when the CO_2 filling of the whole Hele-Shaw cell strongly depends on the height H. However, at early times the diffusive layer is much thinner than the cell height such that the relevant length scale is rather the diffusive thickness $\mathcal{L} = D/\mathcal{U}$, where $D = (1.76 \pm 0.04) \times 10^{-9}\ \mathrm{m^2\ s^{-1}}$ is the diffusivity of CO_2. This dimensionalization has been often used for porous media [3] since the problem is then parameter independent (in the limit of infinite cell height).

The Rayleigh number is defined as

$$\mathrm{Ra} = \frac{K \Delta\rho g H}{\mu D} = \frac{K \alpha \rho_0 k_H P_{CO_2} g H}{\mu D}. \tag{2}$$

In our experiments, this number is varied over four decades from 10^2 to 10^6. The aspect ratio of the experiment is quantified by the Darcy number defined as

$$\mathrm{Da} = \frac{K}{H^2}. \tag{3}$$

This dimensionless number is varied from 6×10^{-5} to 0.05 in the experiments.

The three-dimensional Overbeek-Boussinesq approximation of the Navier-Stokes (NS) equations and the diffusion equation for the CO_2 concentration are made dimensionless using $\mathcal{U}, \mathcal{L}$ and the saturation concentration at thermodynamic equilibrium $C^+ = k_H P_{CO_2}$. This leads to

$$\frac{1}{\mathrm{S}}\left[\frac{\partial \boldsymbol{u}}{\partial t} + (\boldsymbol{u}\cdot\boldsymbol{\nabla})\boldsymbol{u}\right] = -\boldsymbol{\nabla} p - \frac{1}{\mathrm{DaRa}^2} c\,\hat{\boldsymbol{z}} + \Delta\boldsymbol{u}, \tag{4}$$

$$\boldsymbol{\nabla}\cdot\boldsymbol{u} = 0, \tag{5}$$

and

$$\frac{\partial c}{\partial t} + (\boldsymbol{u} \cdot \boldsymbol{\nabla})\, c - \Delta c = 0. \tag{6}$$

These equations are completed by no-slip boundary conditions at the top ($z = 0$) and the bottom ($z = -\mathrm{Ra}$) of the cell. The concentration must satisfy $c = 1$ at the top of the cell and a no-flux condition ($\partial c/\partial z = 0$) at the bottom of the cell. In our experiments, the Schmidt number $\mathrm{S} = \nu/D$ is about 550 and will be considered as infinite in the following. This removes the inertia term, which may become important at very large Rayleigh numbers. Martin *et al.* [25] showed that the full Navier-Stokes-Darcy model with the inertia term works better than the Darcy-Brinkman model for low Schmidt number. This term has been considered in the discussion of Sec. III F but it is neglected (due to the large Schmidt number of the experiments) in the core of the paper.

In order to derive the linear growth rate of the instability, the pressure and concentration fields are expanded around the nonconvective (hydrostatic) solution $[c^{(0)}(z,t), p^{(0)}(z,t)]$. Furthermore, the flow is assumed to be parallel to the (x,z) plane with a parabolic transverse profile (along the y direction) such that Eqs. (5) and (6) can be integrated along the y direction, leading to the two-dimensional Darcy-Brinkman equations:

$$-\boldsymbol{\nabla}_{\parallel} \bar{p} + (\mathrm{DaRa}^2 \Delta_{\parallel} - 1)\bar{\boldsymbol{u}} - \bar{c}\hat{\boldsymbol{z}} = 0, \tag{7}$$

$$\frac{\partial \bar{c}}{\partial t} + \bar{w}\, \partial_z\, c^{(0)} - \Delta \bar{c} = 0, \tag{8}$$

where $\bar{\boldsymbol{u}}$ and $\bar{c}$ correspond to the mean velocity and concentration and where the pressure has been made dimensionless by scaling to $\mu D/K$. Here, $\boldsymbol{\nabla}_{\parallel} = (\partial/\partial x, 0, \partial/\partial z)$ and $\Delta_{\parallel} = \partial^2/\partial x^2 + \partial^2/\partial z^2$ correspond to the gradient and the Laplacian in the plane of the cell.

The 2D Darcy equations are recovered if the Brinkman term $\mathrm{DaRa}^2 \Delta_{\parallel}$ is neglected. In the Darcy model, the Rayleigh number only plays a role through the boundary condition at the bottom of the cell (at $z = -\mathrm{Ra}$ for this dimensionalization). However, at early stages of the instability, this boundary condition is far from the diffusive layer (for large enough Rayleigh numbers) such that the convection problem is virtually independent of the Rayleigh number [7,34].

It is clear from these equations that the Darcy model is only valid at low values of DaRa^2 when the viscous term $\mathrm{DaRa}^2 \Delta_{\parallel} \bar{\boldsymbol{u}}$ due to shears in the (x,z) plane is much smaller than the viscous term $-\bar{\boldsymbol{u}}$ due to the shear in the y direction. It should also be noted that the Darcy-Brinkman model is only valid when the transverse profile is close to parabolic (see the discussion by Zeng *et al.* [20] on the Brinkman's approximation). The goal of this paper is thus to characterize the influence of the Brinkman term $\mathrm{DaRa}^2 \Delta_{\parallel}$ on the characteristics of the instability and to determine experimentally in which range of Rayleigh and Darcy numbers this model is valid.

III. CHARACTERISTICS OF THE INSTABILITY

A. LIF visualizations

As stated above, we used a fluorescent dye to detect the destabilization of the initial purely diffusive profile. A typical sequence of destabilization recorded for $\mathrm{Ra} = 2.4 \times 10^4$ ($P_{\mathrm{CO}_2} = 0.8$ bar and $E = 2$ mm) is presented in Fig. 2. The destabilization process can be generically divided into three stages. First the 1D diffusion of the acid denser layer is observed (stage I). After a period of time which depends on the Rayleigh number, an unstable wavelength $\lambda^\star = 2\pi/q^\star$ emerges, which keeps growing in amplitude until the end of the linear regime (stage II). In the subsequent nonlinear regime, the growth speed of the instability amplitude slows down and the number of fingers decreases through a pairing process during which two adjacent fingers can merge to form a bigger one (stage III). The nonlinear pairing regime then gives birth to a highly aperiodic phase. In this phase (not represented in Fig. 2), the plumes (we call plumes the laterally localized vertical flow observed once a finger has reached the bottom wall of the cell) start merging with their immediate neighbors. The

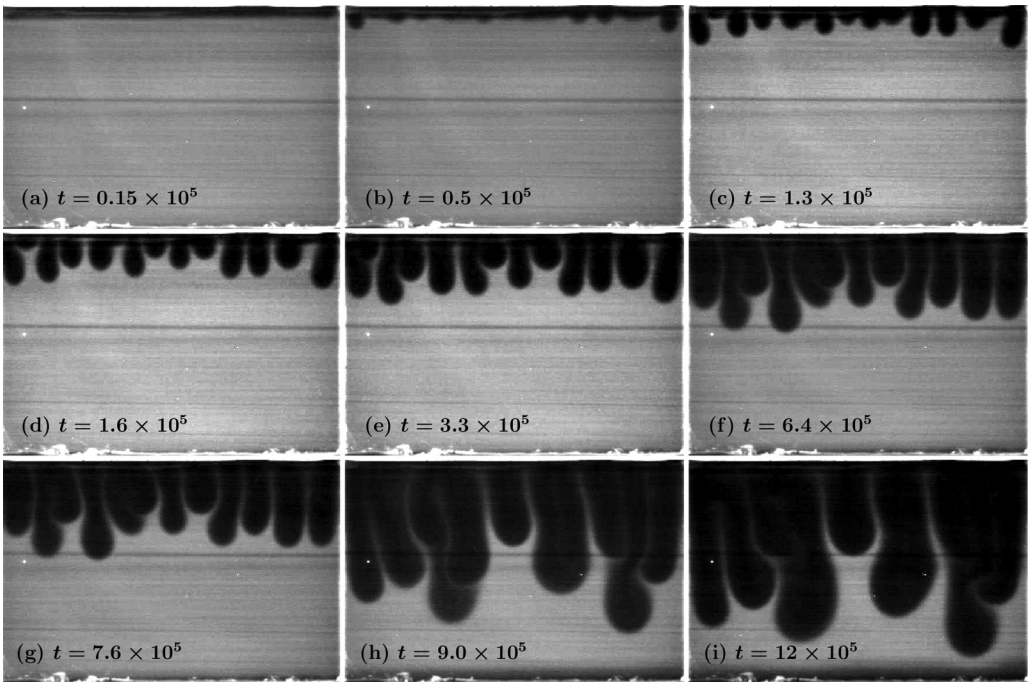

FIG. 2. Sequence of images illustrating the whole fingering process. (a) Pure 1D diffusion regime (stage I); (b)–(c) linear regime (stage II); (d)–(i) nonlinear growth and pairing phenomenon (stage III). Ra $= 2.4 \times 10^4$, Da $= 2.1 \times 10^{-4}$ ($E = 2$ mm and $P_{CO_2} = 0.8$ bar).

room left by the merged plumes allows for the emergence of a new finger, which grows to form a new plume, which in turn can merge with a neighboring plume, and so on. The same steps have been already described in detail by Slim *et al.* [18]. In this paper, we focus on the first two stages where the evolution of the perturbation is essentially linear.

B. Extraction procedure of the experimental quantities

We now describe the method used for the quantitative extractions of the growth rate $\sigma^\star$ and the most unstable wave number $q^\star$ from a typical sequence of images such as the one presented in Fig. 2. We recall that all the variables are dimensionalized (using $\mathcal{U}$ and $\mathcal{L}$); the star only denotes the most probable quantity. We are first interested in the border of the instantaneous concentration field of the perturbation. This front is defined as the limit between the dark (acid) and the lighter (neutral) zone of the picture at t. To be more specific, its position $z_F(x,t)$ corresponds to the position at which the intensity reaches $(\mathcal{I}_{\max} + \mathcal{I}_{\min})/2$ when scanning vertically each pixel column ($\mathcal{I}_{\min}$ and $\mathcal{I}_{\max}$ being respectively the average intensities of the initial and final pictures of the sequence). The amplitude of the fingers is measured by the standard deviation of z_F

$$\mathcal{A}(t)^2 = \overline{z_F(x,t)^2 - \overline{z}_F(t)^2}, \tag{9}$$

where the overline denotes the average over x. The typical shape of the amplitude $\mathcal{A}$ as a function of time is presented in Fig. 3(a). The curve shows a decrease at early times due to the decay of spurious initial perturbations (up to $t = 3 \times 10^5$). The amplitude is then constant and equal to the uncertainty coming from the noise in the images. At $t = 6 \times 10^5$ the amplitude starts to increase with a clear exponential growth over one decade as shown on the semilog plot of Fig. 3(b). The slope can be extracted accurately, leading to an experimental determination of the growth rate $\sigma^\star$ with an uncertainty of the order of 20%. It should be noted that this measurement is made during the linear

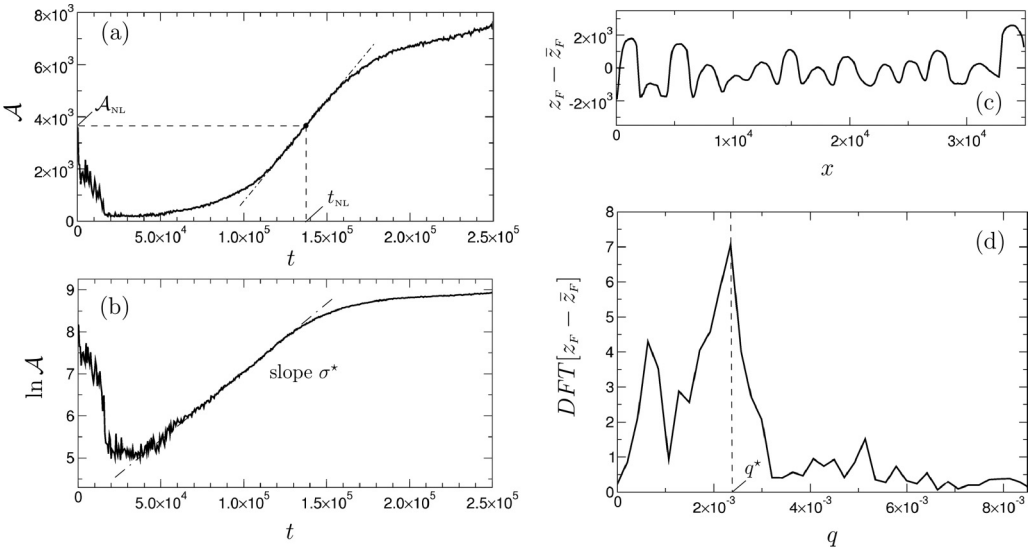

FIG. 3. (a) Lin-lin plot of the rms amplitude of the perturbation as a function of time. The inflexion point on the curve $\mathcal{A}(t)$ is considered as the end of the linear stage. (b) Semilog plot of the rms amplitude of the perturbation as a function of the time. The growth rate $\sigma^\star$ is given by the slope of the linear part of the curve. (c) Position of the front $z_F(x,t_{NL})$ as seen on the LIF visualizations. (d) Discrete Fourier transform of the position of the front. Ra $= 2.4 \times 10^4$, Da $= 2.1 \times 10^{-4}$ ($E = 2$ mm and $P_{CO_2} = 0.8$ bar).

regime and before the pairing of the fingers. The amplitude then saturates, leading to an inflexion point at a time t_{NL}, which will be considered as the end of the linear regime. This time is also clearly identified with an error of the order of 20%.

The quantity $z_F(x,t) - \overline{z}_F$ is plotted in Fig. 3(c) as a function of the spatial coordinate x, at $t = t_{NL}$. Its Discrete Fourier transform (DFT), which is plotted below [Fig. 3(d)], shows a sharp peak located at the most observable wave number $q^\star$. Whenever possible, the most observable wave number $q^\star$ is determined using the DFT of $z_F - \overline{z}_F$. However, in the case of very low Rayleigh numbers (smaller than 1000), the contrast between the dark and the light zones is quite poor and the border is not well defined, so the subsequent analysis is unsatisfactory. For very high Rayleigh numbers (thick cells and high pressures), the border is extremely sharp but there is a background parabolic flow in the x direction, which corrupts the harmonicity of the border. Indeed, as shown in Fig. 4, the fingers tend to gather at the center of the cell since they are advected by a weak recirculation generated by the background parabolic flow. The wavelength is thus smaller at the center than at the sides, leading to a broadening and a flattening of the DFT peak. In such cases, the DFT spectrum is too noisy and the only solution to obtain the most observable wave number $q^\star$ is simply to count the number of fingers in the x direction. Though the procedure is approximate, the experiment gives reproducible results, so that the average value can be trusted within 15% (which is the standard deviation over five different runs). Moreover, the result given by the DFT is in excellent agreement with the one found by counting the number of fingers at intermediate Rayleigh numbers.

C. Growth rate of the instability

Experimental growth rates are plotted in Fig. 5(a) as functions of the Rayleigh number over four decades in Ra. Each point corresponds to an average value over five different runs performed in the same conditions. At low Rayleigh numbers, the growth rate seems to be independent of the Rayleigh number, as should be obtained in the Darcy regime. In order of magnitude, these values (for Ra smaller than 1000) are in excellent agreement with all the numerical and theoretical results listed in

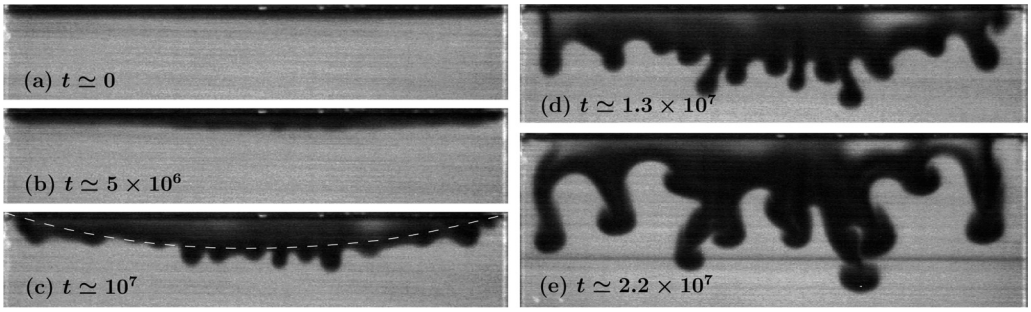

FIG. 4. Sequence of images illustrating the process of destabilization for $\mathrm{Ra} = 8 \times 10^5$ and $\mathrm{Da} = 1.3 \times 10^{-3}$ ($E = 5$ mm and $P_{CO_2} = 6.4$ bar). In this case, the extraction of the wave number $q^\star$ cannot be performed by means of the DFT. We simply count the number of emerging protrusions and get an approximative value. The parabolic flow (white dashed line) is removed (filtered) before performing the rms procedure used to extract the growth rate.

Refs. [4,10]. For example, the value given by Elenius *et al.* [3] is plotted as a dashed line and falls very close to the experimental result at low Rayleigh number.

However, at larger Rayleigh numbers, it is clear that $\sigma^\star$ strongly decreases with the Rayleigh number. Moreover, this decrease seems to depend on the Darcy number. For example, the growth rate at $\mathrm{Ra} = 5 \times 10^4$ is ten times larger at $\mathrm{Da} = 10^{-6}$ than at $\mathrm{Da} = 10^{-3}$. In order to collapse the experimental results, the growth rate is plotted as a function of $\mathrm{Ra}\sqrt{\mathrm{Da}}$ in Fig. 5(b). The experimental results fall on a single curve within 30%. It is interesting to note that the nondimensional parameter $\mathrm{Ra}\sqrt{\mathrm{Da}}$ is equal to $\Delta\rho g E^3/(12\mu D\sqrt{12})$. This parameter can be considered as a Rayleigh number based on the thickness E of the Hele-Shaw cell. This Rayleigh number is independent of the height of the cell H. It is thus the relevant Rayleigh number at early times since the diffusive front is far from the bottom of the cell. This thickness-based Rayleigh number appears naturally in the Darcy-Brinkman equations (7).

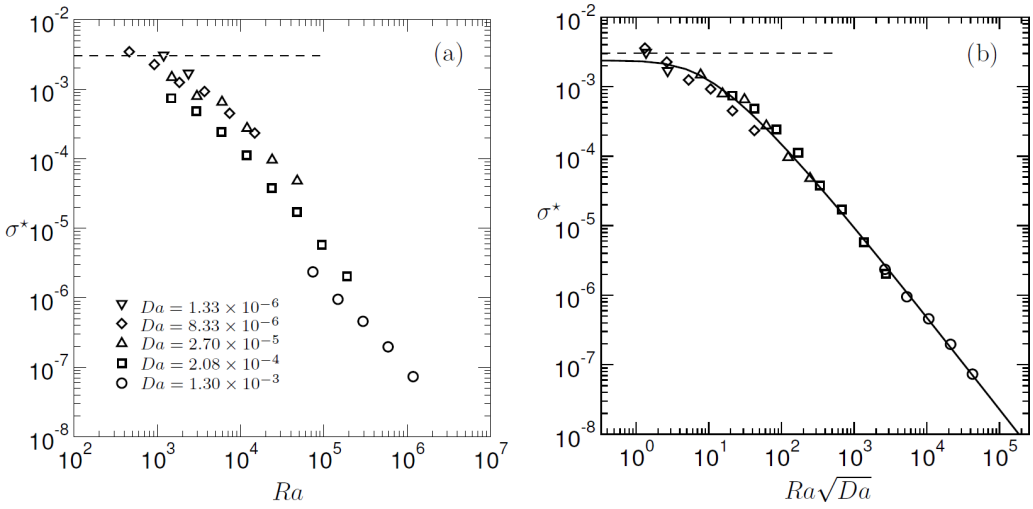

FIG. 5. Growth rate as a function of the Rayleigh number based on the height H (a) and based on the thickness E (b). The experimental data are plotted using open symbols while the theory obtained from Eqs. (10) and (12) is plotted as a solid line. The dashed line corresponds to the numerical prediction of Elenius *et al.* [3] in the Darcy regime.

These experimental results clearly indicate that the Darcy regime is valid up to a value $\mathrm{Ra}\sqrt{\mathrm{Da}} = 1$. Above this value, the Brinkman term creates an additional damping of the velocity, which leads to a decrease of the growth rate. This had already been observed experimentally by Almarcha *et al.* [35] in reactive fronts. However, despite the large number of numerical and theoretical results in the Darcy regime, there is no prediction in the Darcy-Brinkman regime for a diffusive layer. We have modified the analytical result by Fernandez *et al.* [19] to the case of a diffusive layer by taking into account the finite thickness η of the denser layer and by introducing a Gaussian profile of density $c^{(0)}(z,t) = 1 - \mathrm{erf}(z/\eta)$. The details of the calculations are given in the appendix leading to an analytic prediction of the growth rate valid in both the Darcy and the Brinkman regime:

$$\mathrm{Ra}^2\mathrm{Da}\,\sigma = \lambda \mathrm{Ra}^2\mathrm{Da}\,q\left(\frac{1}{1+\coth q\eta} - \frac{q}{\xi+\xi\coth\xi\eta}\right) + 1 - \frac{\lambda q}{\sigma}\left(\frac{1}{1+\coth q\eta} - \frac{q}{\chi+\chi\coth\chi\eta}\right), \tag{10}$$

where

$$\lambda = 0.46, \quad \chi^2 = q^2 + \sigma, \quad \text{and} \quad \xi^2 = q^2 + \mathrm{Ra}^{-2}\mathrm{Da}^{-1}. \tag{11}$$

This theory is valid under the quasi-steady-state approximation (QSSA), which has been shown to give an excellent agreement with the numerical results [7,10] after the onset time. We further use the fact that the linear regime is valid up to times t equal to several σ^{-1}. The thickness $\eta = 2\sqrt{t}$ of the diffusive layer is thus of the order of $\sigma^{-1/2}$ during the linear growth of the instability. It can be approximated by

$$\eta = \frac{A}{\sqrt{\sigma}}, \tag{12}$$

where A is a constant. Introducing this equation in (10) allows us to get an analytical prediction of the most unstable growth rate $\sigma^\star$ and of its corresponding wave number $q^\star$. This prediction is plotted in Fig. 5(b) for a fitting parameter $A = 1$. There is an excellent agreement between the theory and the experiment over the four decades covered by the experiment.

D. Most observable wave number

The most observable wave number $q^\star$ is plotted as a function of the Rayleigh number in Fig. 6. As for the growth rate, the wave number seems to be independent of the Rayleigh number in the Darcy regime [up to $\mathrm{Ra} = 2000$ in Fig. 6(a)]. In order of magnitude, these low Rayleigh experimental results are in good agreement with the values obtained theoretically and numerically in the literature. For example, the onset wave number predicted theoretically by Riaz *et al.* [7] and numerically by Hassanzadeh *et al.* [36] are plotted as dashed and dash-dotted lines respectively. They correspond to an upper bound of our experimental results.

In the Darcy-Brinkman regime, the observed wave number $q^\star$ strongly decreases with the Rayleigh number. It should be mentioned that the experimental results obtained by Outeda *et al.* [15] in this regime are in excellent agreement with our results. As obtained for the growth rate, the experimental results collapse extremely well if the wave number is plotted as a function of $\mathrm{Ra}\sqrt{\mathrm{Da}}$ rather than Ra [see Fig. 6(b)]. This again indicates that the instability only depends on the thickness-based Rayleigh number and is independent of the height H of the Hele-Shaw cell.

The theoretical prediction for $q^\star$ obtained from Eqs. (10)–(12) is plotted as a solid line on Fig. 6(b). The general trend of the experimental data is respected by the theoretical prediction with two different regimes at low and large Ra and a correct scaling law at large Rayleigh numbers. However, the theory clearly overestimates the experimental results. The discrepancy goes from about 20% in the range $10 < \mathrm{Ra}\sqrt{\mathrm{Da}} < 1000$ up to a factor 2–3 for $\mathrm{Ra}\sqrt{\mathrm{Da}} > 1000$. At low Rayleigh numbers ($\mathrm{Ra} \sim 50$) the experimental results are marred by a large uncertainty, making doubtful the

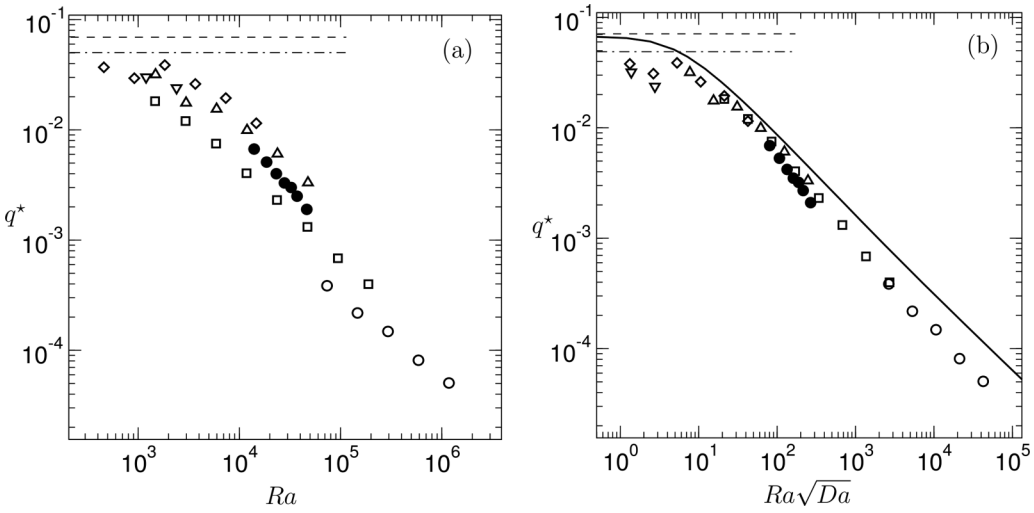

FIG. 6. Most unstable wave number as a function of the Rayleigh number. The experimental data are plotted using open symbols while the theory obtained from Eqs. (10) and (12) is plotted as a solid line. The dashed (resp., dash-dotted) line corresponds to the theoretical (resp., numerical) prediction of Riaz *et al.* [7] (resp., Hassanzadeh *et al.* [36]) in the Darcy regime. The solid circles correspond to the experimental results of Outeda *et al.* [15].

comparison to the theoretical prediction. At moderate Rayleigh numbers, the uncertainty is much smaller, indicating a clear difference between the experiment and the theory. The discrepancy may be explained by the fact that the wave number is estimated at a time t_{NL} later than the onset time. The wave number could have decreased by 20% during this period, as has been observed experimentally [18], numerically, and theoretically [7,8]. The discrepancy could also be due to Taylor dispersion, which may artificially decrease the Rayleigh number, explaining the overestimate of the theoretical prediction.

At large Rayleigh numbers, the discrepancy is much larger and may not be explained by this effect alone. We will show in Sec. III F that it may be due to the failure of the Brinkman's approximation.

Simple scalings can be derived for the theoretical predictions in the large Rayleigh limits. They are calculated rigorously in Appendix B. In the Stokes regime, the growth rate, which scales as $\sigma \sim (q\mathrm{Ra}^2\mathrm{Da})^{-1}$ at large wave numbers (below the cutoff due to molecular diffusion), is damped by the small thickness of the layer for $q < \eta^{-1}$, leading to a most unstable wave number $q^\star$ proportional to η^{-1}. Using the criterion $\sigma \sim \eta^{-2}$ of Eq. (12) and the Stokes value of the growth rate leads to the scalings at large Ra:

$$\sigma^\star \sim \mathrm{Ra}^{-4/3}\mathrm{Da}^{-2/3} \quad \text{and} \quad q^\star \sim \mathrm{Ra}^{-2/3}\mathrm{Da}^{-1/3} \quad \text{for Ra} \to \infty. \tag{13}$$

The last point to be discussed is the upper limit that bounds the Darcy regime. Figures 5 and 6 indicate that the Darcy regime is valid up to $\mathrm{Ra}\sqrt{\mathrm{Da}} = 10$. This corresponds to a dimensional wavelength of the instability equal to approximately twice the cell thickness E. This is consistent with the fact that the Brinkman term becomes dominant above this threshold since the second derivative of the velocity in the x and z directions becomes larger than in the y direction (if the parabolic velocity profile is approximated by half a wavelength of a sine profile).

E. Onset time of the nonlinear regime

The nonlinear time t_{NL} [defined in Sec. III B and in Fig. 3(b)] is plotted in Fig. 7 as a function of the Rayleigh number. Not surprisingly, the nonlinear time is roughly constant for $\mathrm{Ra} < 2000$ in our experiments. For larger Rayleigh numbers, the nonlinear time t_{NL} strongly increases and depends on

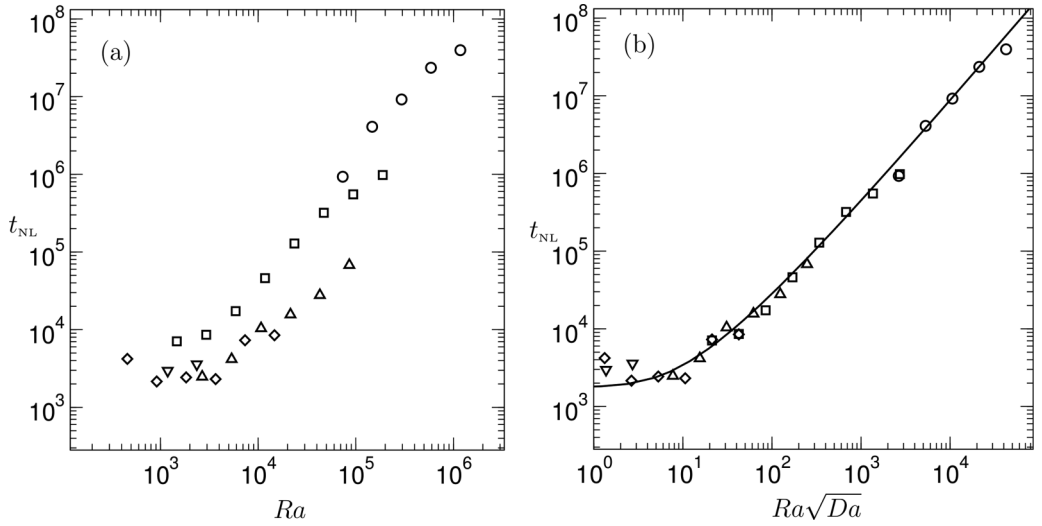

FIG. 7. Observation time $t_{\rm NL}$ as defined in Sec. III (cf. Fig. 3). This time is much greater than the time $\tau^\star$. The theoretical curve (dashed line) corresponds to a product $\sigma^\star t_{\rm NL} = 4.3$, which means that the amplitude of the initial perturbation has grown by a factor about 10^5.

the thickness-based Rayleigh number $\mathrm{Ra}\sqrt{\mathrm{Da}}$ only. We superimposed to the experimental data the theoretical curve obtained by assuming that the nonlinear time $t_{\rm NL}$ is proportional to the characteristic growth time, i.e., $t_{\rm NL} = B/\sigma^\star$, where B is a fitting constant. Using $B = 4.3$ leads to an excellent agreement between theory and experiment in both the Darcy and the Darcy-Brinkman regime. Such a value corresponds to a magnification of the initial perturbation of a factor 70 between the onset time $\tau^\star$ and the observation time (assuming $t_{\rm NL} \gg \tau^\star$).

This value of the nonlinear time is interesting because it gives the value of the saturation time of the instability in a real experiment. This time is very close to the time at which the flux of CO_2 becomes constant as shown numerically [3] and experimentally [18]. This time cannot be predicted numerically or theoretically since it depends on the initial amplitude of the perturbation. Indeed, it may be varied by a factor 15 if the initial amplitude of the perturbations is varied from 0.1 to the numerical noise 10^{-15}. It is thus important to rely on real experiments to get an approximate value of $t_{\rm NL}$. The value estimated in this work is about twice larger than in the experiments by Slim *et al.* [18]. This can be explained by an initial amplitude of the perturbations about 8 times larger in Slim *et al.* [18]. Assuming that our value (resp., Slim's value) is a lower (resp., upper) bound for the initial amplitude of the perturbations in a real aquifer allows us to give a correct estimate (within 25%) of the nonlinear onset time.

F. Validity of the Brinkman's approximation

Despite the simplicity of the crossover argument $\sigma^\star \eta^2 \sim O(1)$, the theoretical results agree fairly well with the experimental data. The general trend of the experimental growth rate is very well reproduced by the theory. The conclusions concerning the most unstable wave number are a bit more mitigated. At low Rayleigh numbers, the extraction of $q^\star$ is not easy, owing to the predominance of the molecular diffusion and the disturbing effect of the remanent convection. Consequently, the results are marred by a large uncertainty. For instance, at $\mathrm{Ra}\sqrt{\mathrm{Da}} = 1.5$, the results obtained for each of the five runs are spread over half a decade. Conversely, results obtained for $\mathrm{Ra}\sqrt{\mathrm{Da}} > 5$ can be considered as accurate within 15%. In the range $10 < \mathrm{Ra}\sqrt{\mathrm{Da}} < 1000$, the difference between theory and experiments is 30% at most. Beyond $\mathrm{Ra}\sqrt{\mathrm{Da}} \sim 1000$ however, the gap increases to reach a factor of 2–3 at $\mathrm{Ra}\sqrt{\mathrm{Da}} = 4 \times 10^4$. This discrepancy cannot be explained only by the uncertainty.

In the previous analysis, the inertia term $\partial \boldsymbol{u}/\partial t$ has been neglected in the equations because it is divided by the Schmidt number. When the growth rate is large (i.e., at large Rayleigh numbers) this term may not be negligible. Martin *et al.* [25] showed that in this case, averaging the Navier-Stokes equation over the cell width leads to 2D Navier-Stokes-Darcy equations:

$$\frac{\mathrm{DaRa}^2}{\mathrm{S}}\frac{\partial \boldsymbol{u}}{\partial t} = -\boldsymbol{\nabla}_{\parallel}\bar{p} + (\mathrm{DaRa}^2\Delta_{\parallel} - 1)\bar{\boldsymbol{u}} - \bar{c}\hat{\boldsymbol{z}}. \tag{14}$$

The acceleration term slightly modifies the equation for the perturbation but can still be solved analytically. It simply introduces a factor $\alpha = 1 + \sigma \mathrm{DaRa}^2/\mathrm{S}$, which is equal to one for small growth rates or high Schmidt number. Solving the equations for the growth rate using the same criterion as before leads to an improved theory, which is always close to the previous theory within 1%. To conclude, this term cannot explain the discrepancy between the theory and the experiments at large Rayleigh numbers.

In order to understand this discrepancy, we performed a systematic PIV analysis of the transverse flow (y direction for $\mathrm{Ra}\sqrt{\mathrm{Da}}$ in the range $[20, 4 \times 10^4]$. The transverse profiles observed below $\mathrm{Ra}\sqrt{\mathrm{Da}} = 700$ are clearly parabolic all over the linear phase of the destabilization process, as illustrated in Figs. 8(a) and 8(b). Beyond this value ($\mathrm{Ra}\sqrt{\mathrm{Da}} > 700$) the transverse profile is not parabolic anymore, but shows some recirculating zones (violation of Brinkman's assumption) as if there were more than one unique finger in the thickness. As shown by Zeng *et al.* [20], this is due to the fact that the wavelengths of the flow are not large enough compared to the cell thickness, which introduces corrections to the velocity profile. An intuitive correction may be added to the theory by considering the three-dimensional situation with a wave number q_y in the y direction. In this case, the Rayleigh number is connected to the value of a *three-dimensional* most unstable wave number $q^\star = (q_x^2 + q_y^2)^{1/2}$. At low Rayleigh numbers, the profile in the gap direction is parabolic which can be modeled as a sine profile with a dimensional wave number Q_y equal to π/E (i.e., with half a wavelength in the cell thickness). At larger Rayleigh numbers, we can suppose that when the theoretical wave number $Q^\star$ becomes greater than π/E, the system is able to accept a larger wave number Q_y while keeping the same modulus of the three-dimensional wave number $(Q_x^2 + Q_y^2)^{1/2} = Q^\star$. It first means that the y velocity profile will contain more than one half-wavelength in the transverse direction, as observed in Fig. 8(c). It also means that the wave number Q_x will be smaller than the theoretical value $Q^\star$, which may explain the discrepancy at large Rayleigh numbers in Fig. 6 between experiments and theory.

In nondimensional units, the criterion $Q^\star > \pi/E$ for the breakdown of the parabolic profile becomes $q^\star > (\pi/\sqrt{12})/(\mathrm{Ra}\sqrt{\mathrm{Da}})$. Using the asymptotic solution (B5) for the most unstable wave number $q^\star$, we can deduce that the y-velocity profile can accept more than half a wavelength for $\mathrm{Ra}\sqrt{\mathrm{Da}} > 296$. This explains the fact that the experimental measurements of $q^\star$ depart from the theory by more than 30% above $\mathrm{Ra}\sqrt{\mathrm{Da}} \sim 300$. It is also consistent with the PIV measurements which indicate that the flow ceases to be parabolic for $\mathrm{Ra}\sqrt{\mathrm{Da}} > 700$.

In the literature, the breakdown of the Brinkman instability has been studied for a mean flow within a Hele-Shaw cell or a capillary tube [37,38] on one hand. The breakdown was obtained at smaller values of the Rayleigh number ($\mathrm{Ra}\sqrt{\mathrm{Da}}$ of the order of 10 to 100 at most). However, such flows contain a strong mean flow which accelerates the tilting of the isoconcentrations and the failure of the Brinkman's model. On the other hand, for the Rayleigh-Taylor instability, Fernandez [23] showed numerically that the isoconcentrations are 2D (i.e., independent of y) at $\mathrm{Ra}\sqrt{\mathrm{Da}} = 7$ and three-dimensional at $\mathrm{Ra}\sqrt{\mathrm{Da}} = 700$ (see their Fig. 16). It tends to indicate that the failure of the Brinkman's approximation takes place slightly below $\mathrm{Ra}\sqrt{\mathrm{Da}} = 700$, which is consistent with our findings. It should be noted that their three-dimensional iso-concentrations at $\mathrm{Ra}\sqrt{\mathrm{Da}} = 700$ is not in disagreement with our parabolic profiles obtained at $\mathrm{Ra}\sqrt{\mathrm{Da}} = 700$ since the velocity profile may remain close to parabolic even if the isoconcentrations become three dimensional.

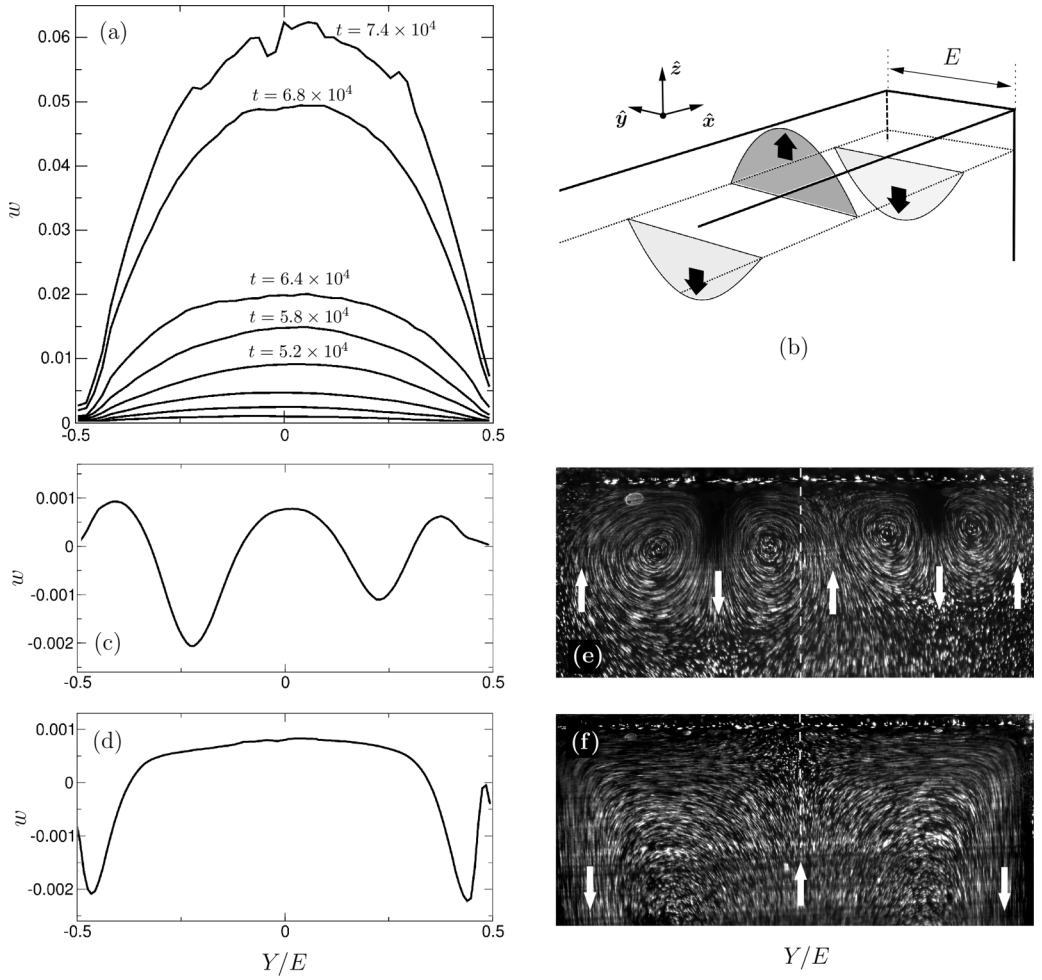

FIG. 8. (a) PIV transverse profile of the vertical velocity obtained for $\mathrm{Ra} = 10^5$, $\mathrm{Da} = 7.5 \times 10^{-5}$ ($E = 1.5$ mm, $P_{\mathrm{CO}_2} = 5$ bar) at $t = 3.7 \times 10^4$, $t = 4.2 \times 10^4$, and $t = 4.8 \times 10^4$, $t = 5.2 \times 10^4$, $t = 5.8 \times 10^4$, $t = 6.4 \times 10^4$, $t = 6.8 \times 10^4$, and $t = 7.4 \times 10^4$. (c), (d) PIV transverse profile of the vertical velocity observed for $\mathrm{Ra} = 9.3 \times 10^5$, $\mathrm{Da} = 1.3 \times 10^{-3}$ ($E = 5$ mm, $P_{\mathrm{CO}_2} = 5$ bar) at $t = 8 \times 10^6$ and $t = 11 \times 10^6$ respectively. (e), (f) Visualization of the corresponding flows obtained by superimposing 20 successive images. Between panels (e) and (f) the two rolls located closest to the vertical walls have shrunk and eventually disappeared. For convenience, the Y coordinate is dimensionalized using E instead of $\mathcal{L}$.

IV. CONCLUSION

The present work was dedicated to the experimental study of the onset of the gravitational instability triggered by the dissolution of carbon dioxide in an aqueous solution. The interest of the paper is mainly experimental since the theoretical technique—i.e., quasi-steady-state approximation to assess the growth rate $\sigma^\star$—that we used as an attempt to interpret the experimental results is classical material. We report an exhaustive exploration of the range $[10^2, 10^6]$ in Rayleigh number allowed by varying the partial pressure of carbon dioxide and the thickness E of the Hele-Shaw cell. Because the gravitational instability is sensitive to small temperature changes, we had to eliminate the temperature rise due to adiabatic intake of the gas. This difficulty was circumvented by means

of a buffer reservoir which initially contained carbon dioxide at the same pressure as the one in the cubic cell, in which pure nitrogen was initially injected.

We measured the growth rate of the instability and the corresponding wave number by means of laser-induced fluorescence. Three regimes in terms of Rayleigh number have been observed: a Darcy regime, the upper bound of which is $\mathrm{Ra}\sqrt{\mathrm{Da}} \sim 10$, where the most unstable wavelength and the growth rate are independent of the Rayleigh number; a so-called Brinkman regime, which lies in the range $\mathrm{Ra}\sqrt{\mathrm{Da}} \in [10, 10^3]$, where Brinkman's approximation is valid; and a high-Rayleigh-number regime, where our theoretical approach seems sufficient to render properly the growth rate of the instability but fails to reproduce the experimentally most unstable wavelength. Such a discrepancy is not rigorously explained, but PIV measurements in the transverse thickness of the cell show that the transverse profile of the convective flow is no longer parabolic beyond $\mathrm{Ra}\sqrt{\mathrm{Da}} \sim 700$.

The careful comparison between experimental results and theoretical analysis done in this paper indicates that the quasi-steady-state approximation (QSSA) is valid within a choice of the one disposable constant A. This permits us to predict the growth and saturation of the instability with a simple analytic formula. It is true that this semiquantitative theory is not able to predict exactly the critical time at which the gravitational instability starts. However, this may be sufficient for most applications since the transport of CO_2 is probably weakly sensitive to the early stages of the instability and to the exact value of the critical time. The transport of CO_2 may be more affected by the late stages of the instability which are governed by the growth rate and the nonlinear saturation time of the instability.

In the future, it would be interesting to study how this Darcy-Brinkman regime modifies the advection and the mixing of a scalar such as CO_2 in a Hele-Shaw cell or in a porous medium. Another interesting extension of this work would be to consider the three-dimensional case of the gravitational instability of a diffusing layer, either in a porous medium or in a simple fluid. Indeed, the structure of the boundary layer could be closely related to the structure of the boundary layer in classical Rayleigh-Bénard convection. Although the Rayleigh number is much smaller in these experiments than in classical thermo-convection, the Schmidt number is much larger, which may give useful information for convection models.

APPENDIX A: GRAVITATIONAL INSTABILITY IN BRINKMAN'S APPROXIMATION

This section is dedicated to the derivation of the growth rate equation (dispersion equation) in the scope of Brinkman's approximation. The situation of two semi-infinite media considered by Fernandez *et al.* [19] is adapted to a denser layer of finite thickness. Taking twice the curl of Eq. (7) yields

$$-\Delta_{\parallel}(\mathrm{Ra}^2\mathrm{Da}\Delta_{\parallel} - 1)\,\bar{\boldsymbol{u}} = (\partial_{xz}\hat{\boldsymbol{x}} - \partial_{xx}\hat{\boldsymbol{z}})\bar{c}. \tag{A1}$$

Now, all first-order quantities are sought in the form of a harmonic function of x multiplied by an exponential function of the time and a still undetermined function of z, that is to say $\bar{u}, \bar{w}, \bar{c} \propto f(z)\exp(\mathrm{i}qx)\exp(\sigma t)$. In the previous form, q is the dimensionless wave number and σ is the growth rate of the instability. For sake of simplicity, the z-dependent part of the previous functions are denoted by the same notations as the ones used for the initial [(x,z,t)-dependent] quantity.

Introducing Eq. (8) in the z component of $[\sigma - (D_z^2 - q^2)]$ (A1) yields the general equation which rules the evolution of the z component of the velocity:

$$\left(D_z^2 - q^2\right)\left[\sigma - \left(D_z^2 - q^2\right)\right]\left[\mathrm{Ra}^2\mathrm{Da}\left(D_z^2 - q^2\right) - 1\right]\bar{w} = q^2\bar{w}\,D_z c^{(0)}, \tag{A2}$$

where D_z stands for the differential operator with respect to the variable z. This equation is completed by a suitable set of boundary conditions at the free surface and at $z \to \infty$. First, all the perturbative quantities are expected to vanish at infinity

$$\bar{w} \to 0 \quad \text{for } z \to -\infty. \tag{A3}$$

At the free surface, the vertical velocity $\bar{w}$ vanishes since the interface is motionless. Moreover, the second derivative of $\bar{w}$ also vanishes due to the incompressibility and the slip boundary condition ($D_z\bar{u} = 0$). Finally, the first-order concentration $c^{(1)}$ vanishes at the interface such that the fourth derivative of $\bar{w}$ must also vanish in order to satisfy (A1). The boundary conditions at $z = 0$ are then

$$\bar{w} = D_z^2\bar{w} = D_z^4\bar{w} = 0 \quad \text{at } z = 0. \tag{A4}$$

1. Steplike profile

We now solve the system composed of Eq. (A2) and boundary conditions (A3) and (A4) in the case of a steplike initial profile. For a steady homogeneous layer of finite thickness η, the profile is given at order zero by

$$c^{(0)} = 1 \quad \text{for } -\eta < z < 0, \tag{A5}$$

$$c^{(0)} = 0 \quad \text{for } z < -\eta. \tag{A6}$$

such that $D_z c^{(0)}$ is now a Dirac δ function. In this case, the equation is solved separately in each layer and the system must be completed by additional boundary conditions on $\bar{w}$ at the altitude $z = -\eta$. Integrating Eq. (A2) leads to a discontinuity condition on the fifth derivative of $\bar{w}$:

$$\mathrm{Ra}^2\mathrm{Da}\big[D_z^5 w\big]_{-\eta^-}^{-\eta^+} = -q^2\,\bar{w}(-\eta). \tag{A7}$$

From the latter equation, we deduce that all the derivative of $\bar{w}$ from the fourth order down to the zeroth one are continuous at the border $z = -\eta$:

$$\big[D_z^n w\big]_{-\eta^-}^{-\eta^+} = 0, \quad (n = 0, \ldots, 4). \tag{A8}$$

In each domain (the border being excluded), Eq. (A2) takes on the simple following form:

$$\big(D_z^2 - q^2\big)\big[D_z^2 - (q^2 + \sigma)\big]\big[D_z^2 - (q^2 + \mathrm{Ra}^{-2}\mathrm{Da}^{-1})\big]\bar{w} = 0, \tag{A9}$$

and the solution $\bar{w}_{1,2}$ relative to the top and bottom domains can be written as

$$\bar{w}_1 = A_q \sinh q z + A_\xi \sinh \xi z + A_\chi \sinh \chi z, \tag{A10}$$

$$\bar{w}_2 = B_q \mathrm{e}^{qz} + B_\xi \mathrm{e}^{\xi z} + B_\chi \mathrm{e}^{\chi z}, \tag{A11}$$

where

$$\xi^2 = q^2 + \mathrm{Ra}^{-2}\mathrm{Da}^{-1} \quad \text{and} \quad \chi^2 = q^2 + \sigma. \tag{A12}$$

The solution $\bar{w}_1$ satisfies the boundary conditions (A4) at the free interface and the solution $\bar{w}_2$ satisfies the condition (A3) at infinity. Then, introducing (A10) and (A11) in the remaining boundary conditions (A7) and (A8) leads to a 6×6 linear system on $A_q, \ldots, B_l$. The vanishing determinant of that system corresponds to the nonzero solution and provides the equation which links the growth rate σ to the wave number q:

$$\mathrm{Ra}^2\mathrm{Da}\,\sigma = \mathrm{Ra}^2\mathrm{Da}\,q\left(\frac{1}{c_q} - \frac{q}{\xi\, c_\xi}\right) + 1 - \frac{q}{\sigma}\left(\frac{1}{c_q} - \frac{q}{\chi\, c_\chi}\right), \tag{A13}$$

where

$$c_q = 1 + \coth q\eta, \quad c_\xi = 1 + \coth \xi\eta \quad \text{and} \quad c_\chi = 1 + \coth \chi\eta. \tag{A14}$$

This formula is equal to Eq. (7) of Fernandez *et al.* [19] in the limit of large thickness η (with $c_q = c_\xi = c_\chi = 2$).

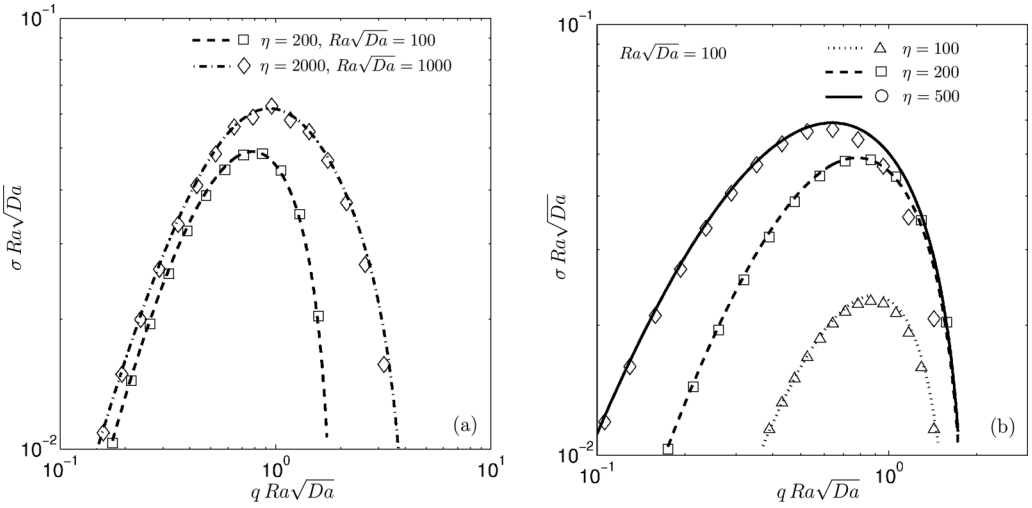

FIG. 9. Growth rate as a function of the wave number (a) for different values of the Rayleigh number (b) for $\mathrm{Ra}\sqrt{Da} = 100$ and different values of η. Results provided by the shooting method are plotted using symbols. Results for the formula (A17) adjusted from the steplike profile with $\lambda = 0.46$ are plotted with lines.

2. Steady diffusion-like profile

We now want to deal with a more realistic zeroth-order profile $c^{(0)}$ which is continuous. Considering the characteristic quantities used to make the problem dimensionless, the nonconvective diffusive profile has a classic form:

$$c^{(0)}(z,t) = 1 - \mathrm{erf}(z/\eta) \quad \text{with} \quad \eta = 2\sqrt{t}. \tag{A15}$$

As time derivative of the zeroth-order profile is not explicitly involved in the first-order system, we numerically solved Eq. (A2) completed by boundary conditions (A3) and (A4) using a numerical shooting method. The solution is searched as the linear combination of three solutions $\bar{w}_q(z)$, $\bar{w}_\xi(z)$, and $\bar{w}_\chi(z)$, which scale as e^{qz}, $e^{\xi z}$, and $e^{\chi z}$ at $z = -\infty$ and which are obtained by numerical integration of (A2) until $z = 0$. A nonzero solution exists, which respects the boundary conditions at the interface, if and only if the determinant

$$\begin{vmatrix} \bar{w}_q(0) & D_z^2\bar{w}_q(0) & D_z^4\bar{w}_q(0) \\ \bar{w}_\xi(0) & D_z^2\bar{w}_\xi(0) & D_z^4\bar{w}_\xi(0) \\ \bar{w}_\chi(0) & D_z^2\bar{w}_\chi(0) & D_z^4\bar{w}_\chi(0) \end{vmatrix} \tag{A16}$$

vanishes. Since these solutions depend implicitly on the growth rate, the searched growth rate is obtained by searching the zero of the determinant. It should be mentioned that the numerical integration is difficult to achieve for a large thickness η (characteristic of large Rayleigh numbers). This is why this method only works for moderate Rayleigh numbers (up to $\mathrm{Ra}\sqrt{\mathrm{Da}} = 1000$).

In Fig. 9(a) is plotted the growth rate σ as a function of the wave number q, for two different values of the Rayleigh number. The presence of molecular diffusion introduces a cutoff at large wave numbers. This cutoff increases with the Rayleigh number, as already shown by Fernandez *et al.* [19].

Figure 9(b) displays the growth rate as a function of the wave number, but for a fixed value of the Rayleigh number $\mathrm{Ra}\sqrt{\mathrm{Da}} = 100$ and different values of the layer thickness η. The finiteness of the thickness η introduces a cutoff at low wave numbers. Moreover, this cutoff changes the scaling of σ at small wave number (see Appendix B).

The curves provided by the shooting method for the so-called real diffusive profile (A15) are plotted with symbols in Fig. 9. The results provided by the semianalytical model of Eq. (A13) for

a steplike profile differ from these numerical results. However, they may be adjusted to fall on the same curve by modifying Eq. (A13) into

$$\mathrm{Ra}^2\mathrm{Da}\,\sigma = \lambda \mathrm{Ra}^2\mathrm{Da}\,q\left(\frac{1}{1+\coth q\eta} - \frac{q}{\xi+\xi\coth\xi\eta}\right)+1 - \frac{q\lambda}{\sigma}\left(\frac{1}{1+\coth q\eta} - \frac{q}{\chi+\chi\coth\chi\eta}\right), \tag{A17}$$

with $\lambda = 0.46$.

This fitting of the analytical curves to the numerical curves is very efficient for all layer thicknesses and Rayleigh numbers since the maximum of the growth rate, its corresponding wave number, and the width of the curves are then identical for the numerical and the analytical results. This analytical prediction is used in the paper to deduce a prediction of the most unstable growth rate and its corresponding wave number in both the Darcy and the Darcy-Brinkman regimes.

APPENDIX B: SCALINGS AT LARGE RAYLEIGH NUMBERS

We explain here the theoretical scalings observed for the growth rate and the wave number at large Rayleigh number. At large Rayleigh numbers (actually for $\mathrm{Ra}^{1/3} \gg q$, the growth rate equation (10) simplifies to

$$\sigma = \lambda q\left(\frac{1}{c_q} - \frac{q}{\xi\, c_\xi}\right). \tag{B1}$$

When the wave number vanishes (limit $q \to 0$), a Taylor expansion of equation (B1) gives

$$\sigma = \frac{\lambda q^2\eta^2}{\mathrm{Ra}\sqrt{\mathrm{Da}}}, \tag{B2}$$

which corresponds to approximation 1 in Fig. 10.

The large wavenumber regime can also be studied by assuming that $q\mathrm{Ra}\sqrt{\mathrm{Da}}$ tends to $+\infty$ while $q\eta$ remains finite. In this case, a Taylor expansion of Eq. (B1) gives

$$\sigma = \frac{\lambda}{2q\mathrm{Ra}^2\mathrm{Da}}\frac{\sinh^2(q\eta)+\sinh(q\eta)\cosh(q\eta)-q\eta}{[\sinh(q\eta)+\cosh(q\eta)]^2}, \tag{B3}$$

This asymptotic solution can be further simplified in the limit of small $q\eta$, leading to $\sigma = \lambda q\eta^2/(2\mathrm{Ra}^2\mathrm{Da})$ which is plotted as the approximation 2 in Fig. 10. Finally, in the limit of large $q\eta$, this asymptotic solution leads to $\sigma = \lambda/(4q\mathrm{Ra}^2\mathrm{Da})$ which is plotted as approximation 3 in Fig. 10.

The maximum growth rate is obtained at the transition between approximations 2 and 3 and is equal to

$$\sigma_\eta \sim \frac{0.1492\lambda\eta}{\mathrm{Ra}^2\mathrm{Da}} \quad \text{at} \quad q_\eta \sim \frac{0.897}{\eta}. \tag{B4}$$

Then, the condition $\sigma^\star\eta^{\star 2} \sim 1$ clearly indicates that the maximum growth rate $\sigma^\star$ and its corresponding wave number $q^\star$ scale as $(\mathrm{Ra}\sqrt{\mathrm{Da}})^{-4/3}$ and $(\mathrm{Ra}\sqrt{\mathrm{Da}})^{-2/3}$ respectively. Introducing these scalings together with the condition $\sigma^\star\eta^{\star 2} = 1$ into (A17), doing a Taylor expansion at large $\mathrm{Ra}\sqrt{\mathrm{Da}}$, and maximizing over q leads to the asymptotic value of the growth rate and of its corresponding wave number,

$$\sigma^\star \sim 0.1061(\mathrm{Ra}\sqrt{\mathrm{Da}})^{-4/3} \quad \text{and} \quad q^\star \sim 0.1361(\mathrm{Ra}\sqrt{\mathrm{Da}})^{-2/3}, \tag{B5}$$

observed on the theoretical curves presented in Figs. 5 and 6, respectively.

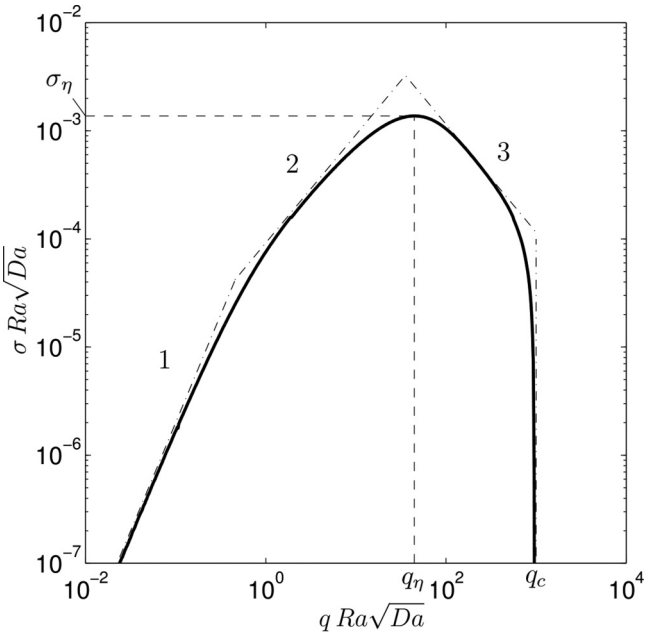

FIG. 10. Growth rate as a function of the Rayleigh number plotted for $\eta = 2 \times 10^8$ and $\mathrm{Ra}\sqrt{\mathrm{Da}} = 10^{10}$. Scaling laws are valid for large values of the Rayleigh number and fixed value of the thickness η. The maximum growth rate σ_η is defined by the crossover between approximations 2 and 3 (see text). Beyond a cutoff value q_c, no unstable wave numbers exist.

[1] H. E. Huppert and J. A. Neufeld, The fluid mechanics of carbon dioxide sequestration, Annu. Rev. Fluid Mech. **46**, 255 (2014).

[2] G. M. Homsy, Viscous fingering in porous media, Annu. Rev. Fluid Mech. **19**, 271 (1987).

[3] M. T. Elenius and K. Johannsen, On the time scales of nonlinear instability in miscible displacement porous media flow, Comput. Geosci. **16**, 901 (2012).

[4] D. A. S. Rees, A. Selim, and J. P. Ennis-King, *Emerging Topics in Heat and Mass Transfer in Porous Media*, Theory and Applications of Transport in Porous Media Vol. 22, edited by Peter Vadász (Springer, Netherlands, 2008), Chap. 4, p. 85.

[5] J. Ennis-King, I. Preston, and L. Paterson, Onset of convection in anisotropic porous media subject to a rapid change in boundary conditions, Phys. Fluids **17**, 084107 (2005).

[6] X. Xu, S. Chen, and D. Zhang, Convective stability analysis of the long-term storage of carbon dioxide in deep saline aquifers, Adv. Water Resources **29**, 397 (2006).

[7] A. Riaz, M. Hesse, H. A. Tchelepi, and F. M. Orr, Onset of convection in a gravitationally unstable diffusive boundary layer in porous media, J. Fluid Mech. **548**, 87 (2006).

[8] S. Rapaka, S. Chen, R. J. Pawar, P. H. Stauffer, and D. Zhang, Non-modal growth of perturbations in density-driven convection in porous media, J. Fluid Mech. **609**, 285 (2008).

[9] A. C. Slim and T. Ramakrishnan, Onset and cessation time-dependent, dissolution-driven convection in porous media, Phys. Fluids **22**, 124103 (2010).

[10] N. Tilton, D. Daniel, and A. Riaz, The initial transient period of gravitationally unstable diffusive boundary layers developping in porous media, Phys. Fluids **25**, 092107 (2013).

[11] G. S. H. Pau, J. B. Bell, K. Pruess, A. S. Almgren, M. J. Lijewski, and K. Zhang, High-resolution simulation and characterization of density-driven flow in CO_2 storage in saline aquifers, Adv. Water Resources **33**, 443 (2010).

[12] B. S. Jhaveri and G. M. Homsy, The onset of convection in fluid layers heated rapidly in a time-dependent manner, J. Fluid Mech. **114**, 251 (1982).

[13] N. Tilton and A. Riaz, Non-linear stability of gravitationally unstable, transient, diffusive, boundary layer in porous media, J. Fluid Mech. **745**, 251 (2014).
[14] T. J. Kneafsey and K. Pruess, Laboratory experiments and numerical simulation studies of convectively enhanced carbon dioxide dissolution, Energy Procedia **4**, 5114 (2011).
[15] R. Outeda, C. El Hasi, A. D'Onofrio, and A. Zalts, Experimental study of linear and nonlinear regimes of density-driven instabilities induced by CO_2 dissolution in water, Chaos **24**, 013135 (2014).
[16] S. Backhaus, K. Turitsyn, and R. E. Ecke, Convective Instability and Mass Transport of Diffusion Layers in a Hele-Shaw Geometry, Phys. Rev. Lett. **106**, 104501 (2011).
[17] J. A. Neufeld, M. A. Hesse, A. Riaz, M. A. Hallworth, H. A. Tchelepi, and H. E. Huppert, Convective dissolution of carbon dioxide in saline aquifers, Geophys. Res. Lett. **37**, L22404 (2010).
[18] A. C. Slim, M. M. Brandi, J. C. Miller, and L. Mahadevan, Dissolution-driven convection in a Hele-Shaw cell, Phys. Fluids **25**, 024101 (2013).
[19] J. Fernandez, P. Kurowski, L. Limat, and P. Petitjeans, Wavelength selection of fingering instability inside Hele-Shaw cells, Phys. Fluids **13**, 3120 (2001).
[20] J. Zeng, Y. C. Yortsos, and D. Salin, On the Brinkman correction in unidirectional Hele-Shaw flows, Phys. Fluids **15**, 3829 (2003).
[21] H. C. Brinkman, A calculation of the viscous force exerted by a flowing fluid on a dense swarm of particles, Appl. Sci. Res. A **1**, 27 (1947).
[22] K. Walker and G. M. Homsy, A note on convective instabilities in Boussinesq fluids and porous media, J. Heat Transfer **99**, 338 (1977).
[23] J. Fernandez, P. Kurowski, P. Petitjeans, and E. Meiburg, Density-driven unstable flows of miscible fluids in a Hele-Shaw cell, J. Fluid Mech. **451**, 239 (2002).
[24] F. Graf, E. Meiburg, and C. Chatel, Density-driven instabilities of miscible fluids in a Hele-Shaw cell: Linear stability analysis of the three-dimensional Stokes equations, J. Fluid Mech. **451**, 261 (2002).
[25] J. Martin, N. Rakotomalala, and D. Salin, Gravitational instability of miscible fluids in a Hele-Shaw cell, Phys. Fluids **14**, 902 (2002).
[26] A. Vreme, Dynamique d'ingestion et de désorption du gaz carbonique en solution aqueuse, Ph.D. thesis, Université de Reims-Champagne-Ardennes, France, 2015 (unpublished).
[27] F. Nadal, P. Meunier, B. Pouligny, and E. Laurichesse, Stationary plume induced by carbon dioxide dissolution, J. Fluid Mech. **719**, 203 (2013).
[28] E. Guyon, J.-P. Hulin, and L. Petit, *Physical Hydrodynamics* (Oxford University Press, Oxford, UK, 2001).
[29] C. Arcoumanis, J. J. McGuirk, and J. M. L. M. Palma, On the use of fluorescent dyes for concentration measurements in water flows, Exp. Fluids **10**, 177 (1990).
[30] A. D. Britt and W. B. Moniz, The effect of pH on photobleaching of organic laser dyes, IEEE J. Quantum Electron. **8**, 913 (1972).
[31] R. Sjoback, J. Nygren, and M. Kubista, Absorption and fluorescence properties of fluorescein, Spectrochim. Acta, Part A **51**, L7 (1995).
[32] P. Meunier and T. Leweke, Analysis and optimization of the error caused by high velocity gradients in particle image velocimetry, Exp. Fluids **35**, 408 (2003).
[33] A. Hebach, A. Oberhof, and N. Dhamen, Density of water + carbon dioxyde at elevated pressures: Measurements and correlation, J. Chem. Eng. Data **49**, 950 (2004).
[34] J. J. Hidalgo and J. Carrera, Effect of dispersion on the onset of convection during CO_2 sequestration, J. Fluid Mech. **640**, 441 (2009).
[35] C. Almarcha, P. M. J. Trevelyan, P. Grosfils, and A. De Wit, Chemically Driven Hydrodynamic Instabilities, Phys. Rev. Lett. **104**, 044501 (2010).
[36] H. Hassanzadeh, M. Pooladi-Darvish, and D. W. Keith, Scaling behavior of convective mixing, with application to geological storage of CO_2, AIChE J. **53**, 1121 (2007).
[37] C.-Y. Chen and E. Meiburg, Miscible displacement in a capillary tube, part 2: Numerical simulations, J. Fluid Mech. **326**, 57 (1996).
[38] Z. Yang and Y. C. Yortsos, Asymptotic solutions of miscible displacement in geometries of large aspect ratio, Phys. Fluids **9**, 286 (1997).